

13th CIRP Conference on Photonic Technologies [LANE 2024], 15-19 September 2024, Fürth, Germany

# Investigations of weld profiling and intermetallic formation in laser welding of steel-to-aluminium: a multi-physics CFD approach using beam shaping

S. Jabar<sup>a\*</sup>, Q. Hayat<sup>a</sup>, A. Baghbani Barenji<sup>a</sup>, G. Chianese<sup>b</sup>,  
H. R. Kotadia<sup>c</sup>, D. Ceglarek<sup>a</sup> and P. Franciosa<sup>a</sup>

<sup>a</sup>WMG, University of Warwick, Coventry CV4 7AL, UK

<sup>b</sup>Institute of Sciences and Technologies for Sustainable Energy and Mobility (STEMS), National Research Council of Italy, via G. Marconi, Naples, Italy

<sup>c</sup>Liverpool John Moores University, Liverpool L3 3AF, UK

\*Corresponding author. Tel.: +44 7957494204. E-mail address: [sharhid.jabar@warwick.ac.uk](mailto:sharhid.jabar@warwick.ac.uk)

## Abstract

The mechanical properties of steel-to-aluminium laser welded joints are dependent on the interfacial intermetallic compounds (IMCs) and the weld interface area. Recent technological advances in laser beam shaping have shown improvements in keyhole stability, porosity formation, optimisation of weld profiles and reduced interfacial IMCs. This study investigated the effect of keyhole stability which is critical in the formation of IMCs and weld profiles. Multi-physics computational fluid dynamics (CFD) simulations and high-resolution microscopy were used to calibrate the model using various core/ring beam power ratios and study their effect on fluid-flow and microstructural evolution. The wider spot from the ring beam improved keyhole stability, whilst the narrower core beam created instability of the weld pool. This study revealed that the strength of the weld was improved by 16% with a ring-only versus core-only beam and total IMC thickness was reduced by up to 50%.

© 2024 The Authors. Published by Elsevier B.V.

This is an open access article under the CC BY-NC-ND license (<https://creativecommons.org/licenses/by-nc-nd/4.0>)

Peer-review under responsibility of the international review committee of the 13th CIRP Conference on Photonic Technologies [LANE 2024]

*Keywords:* laser welding; steel-to-aluminium welding; computational fluid dynamics (CFD); laser beam shaping; intermetallics (IMCs); weld strength.

## 1. Introduction

The move towards improving vehicle efficiency in the automotive industry mandates lightweighting through adopting hybrid designs, which utilise lighter aluminium alloys such as 5xxx and 6xxx series joined to conventional ferrous alloys [1]. The higher energy consumption producing primary aluminium alloys can be offset by lower exhaust emissions due to the lightweighting [2]. These hybrid constructions require the joining of dissimilar metals, which is challenged by the significant differences in the physical properties of steel and aluminium alloys, leading to the formation of brittle intermetallic compounds (IMCs) [3] and solidification cracking [4,5].

Laser beam welding (LBW) has become a popular technology for fusion joining of dissimilar metals, due to the capability of locally controlling the heat input and hence positively influencing the formation and growth of IMCs [6]. Steel-to-aluminium laser welding has applications in battery manufacturing for electric vehicles (EVs) [4] but is also being explored for other structural applications [2].

Laser beam shaping - through optical insertions, coherent beam combining of multiple beams or tandem beams - is gaining popularity for LBW since it holds the promise to control cooling rates and thermal gradients in and around the molten pool. Although significant research papers have studied the mechanism of IMC(s) formation and characterised their distinctive properties using single Gaussian beams, only a few

attempts have studied the effect of laser beam shaping on IMCs formation and weld geometry. For example, Mohammadpour et al. [7] and Yan et al. [8] independently used superimposed and overlapping laser beams, respectively, to reduce IMC thicknesses. Xia et al. [9] used tandem lasers (parallelly spaced) to reduce IMC thickness and increase homogeneity of the IMC layer at the weld interface. Yuan et al. [10] investigated the effects of twin laser spots on the heat distribution between metals. Jabar et al. [3] used the adjustable-ring mode (ARM) laser and studied the impact of the core/ring power ratio on IMCs formation and mechanical properties during LBW of IF steel to 1050 aluminium.

The use of multi-physics computational fluid dynamics (CFD) has allowed digital replications of various laser processes involving fluid-flow and solidification. This advancement provides valuable information, which is difficult to acquire via experiments alone, as well as the ability to produce predictive models with different laser parameters. For example, Chianese et al. [11] used CFD modelling to investigate the effect of laser beam shaping on the material mixing during LBW of copper-to-steel. The study pointed-out that the optimal selection of ring-to-core diameter and ring-to-core power are key factors affecting the keyhole dynamics and ultimately the material mixing during welding.

This paper aims to study the effect of the ARM laser on the lap-shear strength, weld geometry, material mixing and subsequent IMC formation between laser welded lap joints of DC01 steel to 5251-H22 aluminium alloy. The ARM technology was used to enable three beam shapes, namely core-only, ring-only and mixed (core and ring). Experimental work was coupled with CFD simulations to provide valuable information on optimising the laser welding process. The effect of the three beam shapes were correlated with the lap-shear strength and weld geometry, the two of which being closely linked, and the material mixing and subsequent IMC layer formations (at the weld interface). High-resolution microscopy and CFD simulations were used to complement each other to both quantify and explain the metallurgical and fluid-flow phenomena using laser beam shaping.

## 2. Materials and methods

### 2.1. Materials

The study was performed between a Zn-coated mild steel (DC01) and a 5251-H22 aluminium alloy, both 1.5 mm in thickness. Coupons in 112 (L) × 48 (W) × 1.5 (T) mm were used for welding trials and wiped using acetone before welding. Chemical compositions are given in Table 1.

Table 1: Compositions (in wt. %) of the galvanized mild steel (DC01) and 5251-H22 aluminium alloy used in this study.

DC01 steel	Fe	C	Mn	P	S
	Bal.	<0.12	<0.6	<0.045	<0.045
AA5251-H22	Al	Mg	Fe	Mn	Si
	Bal.	1.7-2.4	<0.5	0.1-0.5	<0.4

### 2.2. Laser beam welding setup

LBW was performed using the beam shaping system enabled by the ARM Coherent fiber laser (Coherent ARM FL10000). This system provided a maximum of 10 kW, with up to 5 kW supplied independently to the core and a ring beam, respectively. The laser beam was focused 0.8 mm above the top of the workpiece surface. The power density distribution of the laser beam was measured with a PRIMES power and focus meter (Primes GmbH, Germany). The laser power was delivered via an optical fiber of 100 and 290  $\mu\text{m}$  in diameter for the core and ring beam, respectively. The fiber was coupled with a Scansonic ALO4-O welding head (Scansonic MI GmbH, Germany) (Fig. 1a). The tested laser beam shapes are shown in Fig. 1c. A fixed speed of 120 mm/s was adopted with linear welding (no oscillation). Table 2 provides the processing parameters, which were used in this study – parameters have been selected to maintain a fixed weld depth penetration ( $W_d$  in Fig. 1b) of approximately 1.7 mm across the 3 welding setups. Welding was limited to a shallow conduction mode on the aluminium side. This was due to its restricted material mixing and relatively thin IMC formation which can be effectively quantified and studied.

Table 2: List of processing parameters and beam shapes used in this study.

Parameter	Core	Ring	Mixed
Speed [mm/s]		120	
Focal offset [mm]		0.8	
Core power [W]	3000	0	2000
Ring power [W]	0	5000	2000

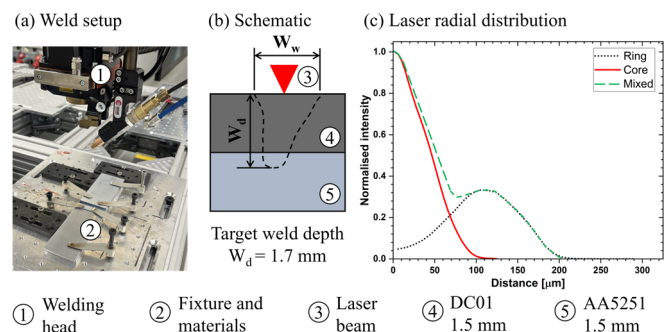


Fig. 1: (a) weld setup, (b) schematic of a typical cross-section and (c) normalised power density distribution.

### 2.3. CFD modelling and assumptions

The multi-physics model was developed using the commercially available CFD software FLOW-3D®, solver version: 12.0.2.01 and its module FLOW-3D® WELD (release: 7, update: 3). The following assumptions were made for the model development:

- the computational fluid domain is assumed Newtonian and incompressible;
- vaporised air and metal from LBW are modelled as a ‘void’, with ambient pressure and temperature;
- any heat sinking effect from the clamping and welding table against the bottom of the bottom sheet is neglected;

- the effect of the plasma plume on the laser absorption is not directly modelled but it is accounted for in the calibration as also presented by [12];
- laser absorption is assumed temperature-dependent, and independent of the incidence angle as also presented by [13];
- loss of material is only associated with material evaporation and not spatters because of the welding process; and,
- the presence of the Zn coating on the steel was not modelled in the simulation.

#### 2.4. Governing equations of the CFD model

The core of the CFD model is the solution for mass, momentum and conservation of energy equations – full formulations can be found in [11]. The following physics have been accounted to model the welding process.

**Tracking of the keyhole** – the surface of the keyhole is tracked by the volume of fluid (VOF) method which enables the calculation of the interface between the liquid metal and the void type, according to equation (1) –  $f$  is the fraction of fluid in each cell (value from 0 to 1) and  $\vec{v}$  is the velocity vector.

$$\partial f / \partial t + \nabla \cdot (\vec{v} f) = 0 \quad (1)$$

The fluid-flow and subsequent mixing are traced in each cell and are tracked by a scalar value  $f_2$ . This indicates the fraction of 2nd material (Al) in each cell. Values of the material property  $\bar{\varphi}$  is evaluated in each cell as a weighted sum of the properties of  $\varphi_1$  and  $\varphi_2$  of the parent materials, as shown in equation (2).

$$\bar{\varphi} = (1 - f_2) \cdot \varphi_1 + f_2 \cdot \varphi_2 \quad (2)$$

**Multiple reflections** - Multiple reflections are implemented using a discrete grid cell system through the ray tracing technique, as defined in equation (3), where  $\vec{R}$  represents the direction of the reflected ray,  $\vec{I}$  represents the direction of the incoming ray, and  $\hat{n}$  signifies the normal direction of the material's surface.

$$\vec{R} = \vec{I} - 2(\vec{I} \cdot \hat{n})\hat{n} \quad (3)$$

**Phase change** – This is modelled as mass transfer between the liquid phase and the void type and proportional to the difference between the saturation pressure  $P_{sat}$  and the partial pressure  $P_{vap}$  (equation (4)) -  $\alpha$  is the accommodation coefficient,  $T$  is the temperature,  $R$  is the gas constant,  $P_{sat}$  is the saturation pressure and  $P_{vap}$  is the partial pressure of the gaseous phase.

$$Q_{mass} = (\alpha / \sqrt{2\pi RT}) \cdot (P_{sat} - P_{vap}) \quad (4)$$

$$P_{sat} = P_v \cdot \exp((\Delta H_v / ((\gamma - 1) \cdot c_v T_v)) \cdot (1 - T_v / T)) \quad (5)$$

The saturation pressure is estimated using the Clausius-Clapeyron relation which is represented by equation (5), where,  $P_v$  and  $T_v$  represent distinct points on the saturation curve,  $\gamma$  represents the specific heat ratio and  $\Delta H_v$  represents the latent heat of vaporisation.

**Recoil pressure** – The recoil pressure can be represented by the equation (6), with coefficients  $A_r$  and  $B$  calibrated based on the experimental results.

$$P_{recoil} = A_r \cdot \exp(B \cdot (1 - T_v / T)) \quad (6)$$

**Surface tension** - The surface tension-related features such as Laplace pressure ( $L_P$ ) and Marangoni forces ( $S_M$ ) also have a significant influence on the laser welding process. These two features can be represented by the equations (7) and (8), where,  $\sigma$  does represent the surface tension and  $R_1$  and  $R_2$  are the principal curvature radii and  $\nabla_t$  represents the gradient along the tangential direction of the interface.

$$L_P = \sigma \cdot (1/R_1 + 1/R_2) \quad (7)$$

$$S_M = \nabla_t \sigma \quad (8)$$

#### 2.5. Computational domain and material properties

The computational domain was divided into two distinct zones as illustrated in Fig. 2. These included a finer mesh zone 1 (Z1) which encompassed the phase change and a coarser mesh zone 2 (Z2) which was defined as a thermal diffusion zone. For Z2 the mesh size was 4 times as greater than Z1, due to the only requirement being to model the heat transfer. Dimensions of Z1 were 10 mm × 2 mm × 2 mm - the length of this zone allowed to achieve a steady state evolution of the welding process. A range of mesh sizes (100, 75, 50, 30 and 20  $\mu$ m) were used to determine a mesh independent solution, resulting in a mesh size of 50  $\mu$ m. The key temperature-dependent material properties for the steel and aluminium were imported from the JMATPRO® database.

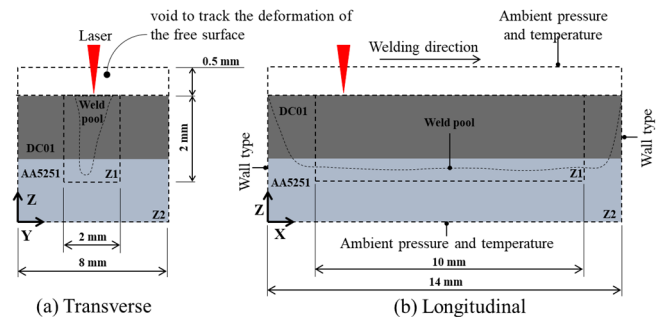


Fig. 2: Schematic representations showing the computational domain (a) transverse and (b) longitudinal.

#### 2.6. Material characterisation techniques

For metallographic sample preparation, cross-sections were taken at 4, 6 and 8 mm to match with those from the CFD simulations. Cross-sections were prepared using standard metallographic procedures. Lap-shear testing of the specimens was performed on an Instron 30 kN tensile testing apparatus at an extension rate of 1 mm/min, for each weld ID, and 3 replications were carried out.

A Keyence VHX7000 light microscope was used to acquire images which were used for quantifying geometrical measurements of the welds. An FEI Versa 3D dual-beam scanning electron microscope (SEM) equipped with energy dispersive x-ray spectroscopy (EDS) was used for chemical-mapping.

Data analysis was performed using the Oxford Instruments AZtec software and SEM operating parameters of 20 kV (accelerating voltage) and 11 nA (current) was used at different

magnifications. Phase differentiation was performed based on the wt. % of the mixed material regions using the built in AutoPhaseMap tool. Quantitative measurements of the IMC thicknesses and weld interface perimeters were also extracted from this data using image analysis software.

### 3. Results and discussion

#### 3.1. CFD model calibration and validation

The CFD model was calibrated against the actual experiment and  $A_r$  and  $B$  parameters from equation (6) were adjusted to match the weld profile and the Fe-Al composition from experiments. Fe-Al compositions along the centre of the weld pool cross-section were used as comparisons between the experimental and simulated welds. The calibration was conducted for each welding setup, “core”, “ring” and “mixed” (core and ring). Through this calibration process, the following values were obtained for  $A_r$  for each of the three setups: 5000 Pa, 400 Pa and 800 Pa, “core”, “ring” and “mixed”, respectively. For  $B$ , the value was fixed to 6.45 for all three setups.

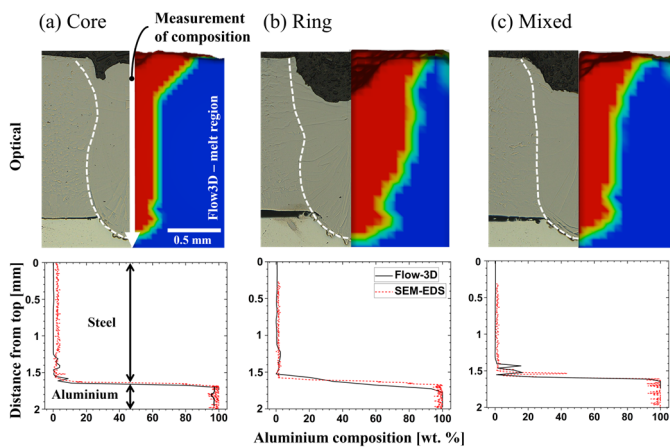


Fig. 3: Model validation showing the optical microscopy and cross-sections of the simulated melt region, with the comparison of SEM-EDS compositions along the centre of the weld.

Fig. 3 shows the comparison between the calibrated CFD simulations and weld experiments. For the weld geometry, weld width and weld depth are in good agreement for all 3 configurations. It should be noted that the model does not consider the effect of part-to-part gap at the interface between the two sheets – this can explain the underfilled concavity, observed in the ring and mixed welds (Fig. 3b – c), which was not accurately reproduced in the CFD models. The composition along the length of the weld is also plotted for each setup. In each instance, there is good agreement, including the finer details on composition changes, which can be seen just before the sharp composition changes at around 1.5 mm for both the core-only and mixed welds (Fig. 3a and 3c).

#### 3.2. Weld interface and mechanical properties

The strength of the three welds were quantified using lap-shear testing (Fig. 4d). The best performing weld was the ring-only with an average lap-shear strength of 92.5 N/mm, this was

followed by the mixed and core-only welds. These differences can be owed to two reasons: (1) the extent of the bonding at the weld interface and (2) the intermetallic formation at the interface.

For the weld interface perimeter, measurements were made as annotated in Fig. 4b. A clear difference was found amongst the three setups, in which the ring-only weld had the largest interface perimeter, followed by the mixed and core-only welds. These differences can be due to the distinct power density distributions of the core and ring lasers, shown in Fig. 1c. Since the ring laser has a wider beam, the width of the weld which penetrated the aluminium is subsequently wider. This correspond to an average 16% higher strength with the ring-only beam compared to core-only beam. Similar results have been found by Jabar et al. [3], who showed that a ring-dominant laser beam setup was effective in providing a more lateral heat distribution, subsequently increasing the interface perimeter and the lap-shear strength.

The reasoning behind the intermetallic formation at the interface is discussed in Section 3.3.

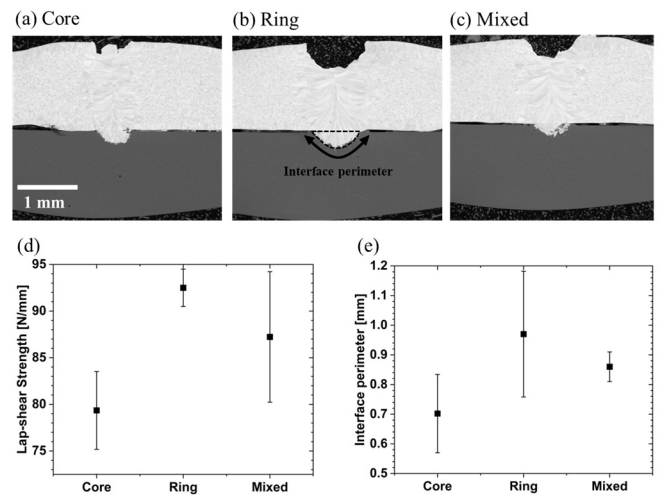


Fig. 4: (a – c) SEM-BSE images of the 3 weld microstructures, (d) lap shear strengths and (e) weld interface perimeter.

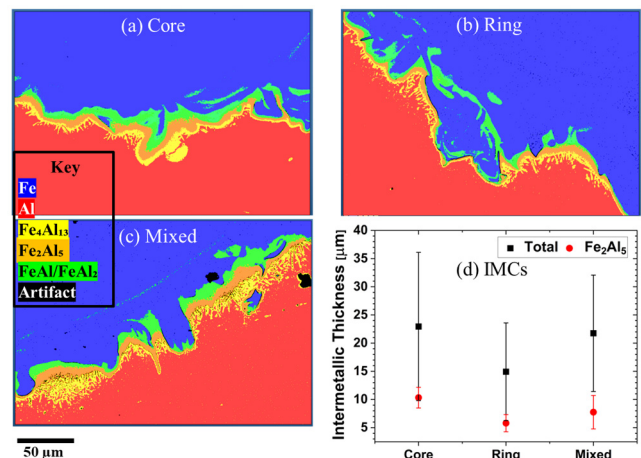


Fig. 5: Comparison of IMC thicknesses at the steel-to-aluminium weld interface for the (a) core-only (b) ring-only and (c) mixed welds. (d) Quantification of the IMC thicknesses.

### 3.3. Fluid-flow and intermetallic formation

The formation of IMCs at the interface between the steel-to-aluminium was quantified between the 3 tested beam shapes (Fig. 5). The different IMC types were characterised based on their composition which can be found from the Fe-Al binary phase diagram [4]. In terms of a ranking, the ring-only weld produced the thinnest IMC layer in a discontinuous layer (Fig. 5b) and Fe<sub>2</sub>Al<sub>5</sub> IMC - the latter is the most brittle [3] and therefore, detrimental to weld integrity. Whereas the core-only beam produced the thickest IMC layer and Fe<sub>2</sub>Al<sub>5</sub> IMC in a thick continuous layer (Fig. 5a), with the mixed weld falling in between the two.

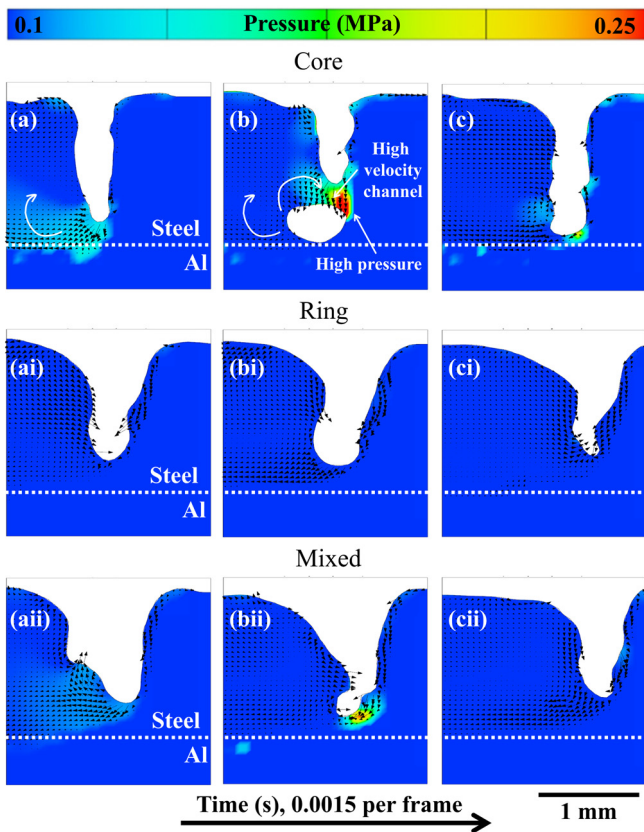


Fig. 6: CFD simulation results showing the pressure distribution in multiple frames of each of the 3 weld setups. Black arrows are representative of the velocity field.

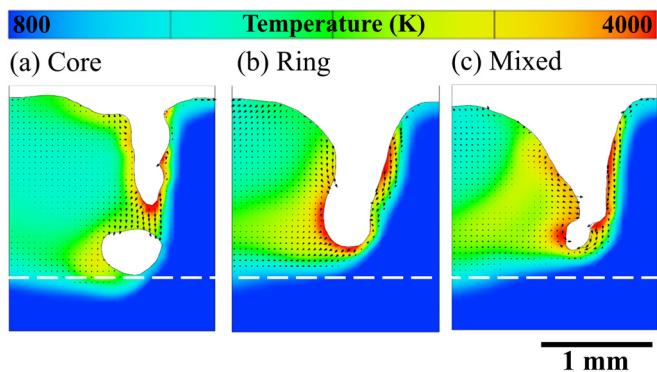


Fig. 7: CFD simulation results (corresponding to the same time frames shown in Fig. 6b-bi-bii) showing the temperature of fluid for each of the 3 weld setups. Black arrows are representative of the velocity field.

The differences in the formation of IMC layer thicknesses can be attributed to the keyhole formation and subsequent fluid-flow as displayed in the frame-to-frame snapshots taken from the CFD simulations (Figs. 6 and 7). The differences in keyhole shape and formation of different features (bubble in the core-only beam) lead to the subsequent differences found in Fig. 5 - the schematic representation in Fig. 8 shows the key effects of the core and ring beams on the weld pool.

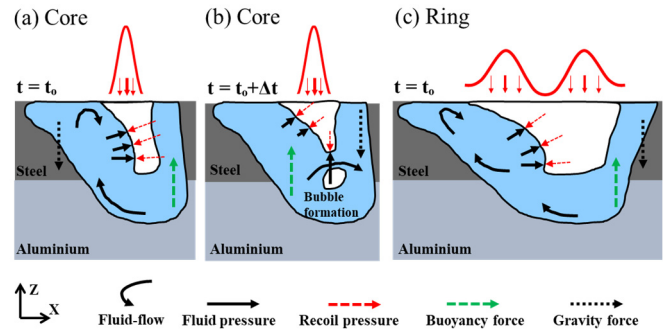


Fig. 8: Schematic representation of the forces and pressures acting on the keyhole and melt pool for the (a and b) 2 consecutive time frame of the core-only beam and (c) ring-only weld.

In the case of the core-only, the narrower beam leads to a narrower keyhole formation and increased fluid pressure on the rear keyhole wall, which restricts release of vapours and forces the keyhole to close (*necking* of the keyhole). This results in the formation of a bubble in the bottom of the keyhole and fluid velocity is very high in the fluid channel above the bubble (Fig. 6b). Closure of the keyhole restricts the ejection of vapors out of the keyhole which leads to an increase in pressure within the keyhole and creates a high-pressure that builds up and focusses on the bottom of the keyhole, creating an extremely high-pressure region as seen in Fig. 6b. The pressure is extremely high in this region which induces a highly turbulent and high velocity in the narrow channel. Together with the higher peak temperature (Fig. 7a), this promotes material mixing with aluminium travelling upwards due to buoyancy forces. This explains the increased material mixing and IMC formation at the core-only interface (Fig. 5a). It should be noted that in the current study the formation of bubbles did not lead to the formation of porosity due to filling of the void or gaseous escape through the part-to-part gaps visible in Fig. 3.

In comparison, for the ring-only weld (Figs. 6ai – ci), the wider beam allows the keyhole to remain open and stable without collapsing. This is due to the lower pressure on the rear keyhole wall, and therefore less turbulent fluid-flow and lower velocity. This prevents the formation of a bubble and accumulation of pressure, leading to a more homogeneous formation of IMCs at the interface (Fig. 5b). Furthermore, the lower pressure and fluid-flow, together with reduced peak temperature (Fig. 7b – c), leads to reduced buoyancy forces. Similarly, for the mixed weld, the influence of the ring beam allowed for a wider and more stable keyhole, although some sign of a near bubble formation was evident in this setup (Fig. 6bii).

Furthermore, the keyhole shapes visible in Fig. 6 can be linked to the weld pool shapes and interface perimeter measurements in Fig. 3 and Fig. 4e, respectively. The width of

the keyholes corresponds to the weld interface characteristics. The wider keyhole in Fig. 6ai – ci leads to a larger weld perimeter, whereas the narrow keyhole in Fig. 6a – c, leads to a smaller weld perimeter. As explained in Section 3.2, this affects the extent of bonding in the weld and overall lap-shear strength.

#### 4. Conclusions

This study investigated the influence of beam shaping on the weld profile and IMCs formation of dissimilar steel-to-aluminium joints during laser beam welding. Complementing CFD simulations and experimental data, three key findings can be drawn from the work, as follows;

- the ring-only beam provided the largest interfacial perimeter at the weld interface due to a wide beam in comparison to the core beam. This in turn created a larger bonding interface which led to the greatest (92.5 N/mm) lap-shear strength of the weld;
- in the core-only weld the thickest total IMC layer was found to be 23.5  $\mu\text{m}$ ; additionally, the thickest  $\text{Fe}_2\text{Al}_5$  IMC layer was 10.5  $\mu\text{m}$ . This was due to the closing of the weld keyhole and formation of a bubble which led to a build-up of pressure and subsequently turbulent fluid-flow leading to more material mixing at the weld interface; and,
- the wider spot of the ring beam meant the keyhole remained open during welding, leading to stability and reduced bubble formation. Overall, this led to the thinnest total IMC layer (15  $\mu\text{m}$  on average), and the thinnest  $\text{Fe}_2\text{Al}_5$  IMC layer (6  $\mu\text{m}$  on average).

The findings highlight the importance of the optimal selection of the core-to-ring shape during LBW of steel-to-aluminium (while in conduction mode on the aluminium side) for controlling the weld profile, increasing the mechanical integrity and reducing interfacial IMCs. Future work will expand on steel-to-aluminium laser welded joints using other laser beam technologies, such as beam oscillation and dynamic beam, to control formation of IMCs and ultimately tailor the weld microstructure.

#### Acknowledgements

This work was supported by (1) WMG High Value Manufacturing Catapult Centre (2) EPSRC JLR iCase voucher 20000095 (Remote Laser Welding of Dissimilar Metals for Automotive Structural Applications) and (3) EPSRC MSI (Research Centre for Smart, Collaborative Industrial Robots) grant number EP/V062158/1. The authors would like to acknowledge the support provided by the WMG Characterisation Facility partially funded by Higher Education Funding Council for England (HEFCE) and the WMG High Value Manufacturing Catapult Centre.

#### References

- [1] Sergey Kuryntsev, "A Review : Laser Welding of Dissimilar Materials," *Materials (Basel)*, vol. 15, no. 122, 2022, doi: <https://doi.org/10.3390/ma15010122>.
- [2] A. Gullino, P. Matteis, and F. D. Aiuto, "Review of aluminum-to-steel welding technologies for car-body applications," *Metals (Basel)*, vol. 9, no. 3, pp. 1–28, 2019, doi: 10.3390/met9030315.
- [3] S. Jabar, A. Baghbani Barenji, P. Franciosa, H. R. Kotadia, and D. Ceglarek, "Effects of the adjustable ring-mode laser on intermetallic formation and mechanical properties of steel to aluminium laser welded lap joints," *Mater. Des.*, vol. 227, 2023, doi: 10.1016/j.matdes.2023.111774.
- [4] S. Jabar et al., "Effect of a ring-shaped laser beam on the weldability of aluminum-to-hilumin for battery tab connectors," *J. Laser Appl.*, vol. 35, no. 04, 2023, doi: 10.2351/7.0001156.
- [5] H. R. Kotadia, P. Franciosa, S. Jabar, and D. Ceglarek, "Remote laser welding of Zn coated IF steel and 1050 aluminium alloy: processing, microstructure and mechanical properties," *J. Mater. Res. Technol.*, vol. 19, pp. 449–465, 2022, doi: 10.1016/j.jmrt.2022.05.041.
- [6] J. Yang et al., "Laser techniques for dissimilar joining of aluminum alloys to steels: A critical review," *J. Mater. Process. Technol.*, vol. 301, no. November 2021, p. 117443, 2022, doi: 10.1016/j.jmatprotec.2021.117443.
- [7] M. Mohammadpour, N. Yazdian, G. Yang, H. P. Wang, B. Carlson, and R. Kovacevic, "Effect of dual laser beam on dissimilar welding-brazing of aluminum to galvanized steel," *Opt. Laser Technol.*, vol. 98, pp. 214–228, 2018, doi: 10.1016/j.optlastec.2017.07.035.
- [8] S. Yan, Z. Hong, T. Watanabe, and T. Jingguo, "CW/PW dual-beam YAG laser welding of steel/aluminum alloy sheets," *Opt. Lasers Eng.*, vol. 48, no. 7–8, pp. 732–736, 2010, doi: 10.1016/j.optlaseng.2010.03.015.
- [9] H. Xia, W. Tao, L. Li, C. Tan, K. Zhang, and N. Ma, "Effect of laser beam models on laser welding-brazing Al to steel," *Opt. Laser Technol.*, vol. 122, no. September 2019, p. 105845, 2020, doi: 10.1016/j.optlastec.2019.105845.
- [10] R. Yuan, S. Deng, H. Cui, Y. Chen, and F. Lu, "Interface characterization and mechanical properties of dual beam laser welding-brazing Al/steel dissimilar metals," *J. Manuf. Process.*, vol. 40, no. January, pp. 37–45, 2019, doi: 10.1016/j.jmapro.2019.03.005.
- [11] G. Chianese, Q. Hayat, S. Jabar, P. Franciosa, D. Ceglarek, and S. Patalano, "A multi-physics CFD study to investigate the impact of laser beam shaping on metal mixing and molten pool dynamics during laser welding of copper to steel for battery terminal-to-casing connections," *J. Mater. Process. Technol.*, vol. 322, no. April, p. 118202, 2023, doi: 10.1016/j.jmatprotec.2023.118202.
- [12] Y. Hao, N. Chen, H. P. Wang, B. E. Carlson, and F. Lu, "Effect of zinc vapor forces on spattering in partial penetration laser welding of zinc-coated steels," *J. Mater. Process. Technol.*, vol. 298, no. July, p. 117282, 2021, doi: 10.1016/j.jmatprotec.2021.117282.
- [13] W. Huang, W. Cai, T. J. Rinker, J. Bracey, and W. Tan, "Effects of laser oscillation on metal mixing, microstructure, and mechanical property of Aluminum-Copper welds," *Int. J. Mach. Tools Manuf.*, vol. 188, no. September 2022, p. 104020, 2023, doi: 10.1016/j.ijmachtools.2023.104020.